

Positive role of the long luminescence lifetime of upconversion nanophosphors on resonant surfaces for ultra-compact filter-free bio-assays

DU C TU VU,^{1,2,3}  THANH-THU VU LE,⁴ CHIA-CHEN HSU,⁴ NGOC DIEP LAI,³ CHRISTOPHE HECQUET,¹ AND HENRI BENISTY^{1,*} 

¹Laboratoire Charles Fabry, CNRS, Institut d'Optique Graduate School, Université Paris-Saclay, Palaiseau, 91127, France

²Faculty of Electrical and Electronics Engineering, Phenikaa University, Yen Nghia, Ha-Dong District, Hanoi, 10000, Vietnam

³Laboratoire Lumière, Matière et Interfaces (LuMI), FRE 2036, École Normale Supérieure Paris-Saclay, 4 Avenue des Sciences, Gif-sur-Yvette, 91190, France

⁴Department of Physics and Center for Nano Bio-Detection, National Chung Cheng University, Ming Hsiung, Chia Yi, 621, Taiwan

*henri.benisty@institutoptique.fr

Abstract: We introduce a compact array fluorescence sensor principle that takes advantage of the long luminescence lifetimes of upconversion nanoparticles (UCNPs) to deploy a filter-free, optics-less contact geometry, advantageous for modern biochemical assays of biomolecules, pollutants or cells. Based on technologically mature CMOS chips for ~10 kHz technical/scientific imaging, we propose a contact geometry between assayed molecules or cells and a CMOS chip that makes use of only a faceplate or direct contact, employing time-window management to reject the 975 nm excitation light of highly efficient UCNPs. The chip surface is intended to implement, in future devices, a resonant waveguide grating (RWG) to enhance excitation efficiency, aiming at the improvement of upconversion luminescence emission intensity of UCNPs deposited atop of such an RWG structure. Based on mock-up experiments that assess the actual chip rejection performance, we bracket the photometric figures of merit of such a promising chip principle and predict a limit of detection around 10-100 nanoparticles.

© 2020 Optical Society of America under the terms of the [OSA Open Access Publishing Agreement](#)

1. Introduction

Fluorescence-based analysis currently evolves from a critical research tool to an enabling technology for the emerging applications of biomedicine ranging from biomedical diagnostics [1,2] and cellular imaging [3] to molecular imaging [4]. In this landscape, compact fluorescence assays are desirable in several contexts, to assist healthcare or research work without impacting the lab's limited real estate [5–8]. Handheld devices enable point-of-care testing, capable of delivering diagnosis results rapidly, easily and accurately near patient's bedside, doctor's surgery, emergency room or intensive care unit [9,10]. The huge achievements of fluorescence microscopies have most often required bulky high performance microscopes, or some still bulky optics to visualize useful features on chips such as “fluorescence spots” or individual cells. The direct contact geometry [11] using detection on a CCD or CMOS sensor chip (whose performances are nowadays very good) is much less bulky and close to the lower limit that can be devised: only illumination must be brought to the chip either in some innovative integrated fashion or with any ordinary small-size optics: small LED illuminators and light pipes, small laser heads, fiber head for remote lasers. A very thin glass bottom (say 100 μm) can limit the blurring on the short path to the chip and grant reasonable images for spots down to 200 μm diameter. Furthermore, a glass-based faceplate (polished fiber bunch) can serve as an angular

filter (typically selecting $\text{NA} \lesssim 1$) that limits blurring and relaxes various mechanical constraints [7,12].

A daunting challenge when targeting ordinary down-conversion luminescence signals in an optical assay/sensor contact geometry is to implement the mandatory excitation rejection [5,11–13]. A huge rejection factor is needed to limit residual excitation detection below the noise floor. To do this, a filter inserted between the chip and the sensor blurs direct imaging for extra thicknesses as small as 70 μm . It is known that good filters work on absorption rather than on multilayer, but then suffer from a residual autofluorescence and also feature a substantial thickness [12,13]. These factors make the insertion of a rejection filter a very delicate task. A mitigation is to use fluorescent species with giant Stokes shift such as red-emitting quantum dots excited around $\lambda = 400 \text{ nm}$, as the large shift $\lambda_{\text{fluor}} - \lambda_{\text{exc}} = \Delta\lambda_{\text{Stokes}} \gtrsim 200 \text{ nm}$ makes high rejection obtainment a lot easier than the classical 50–80 nm Stokes shift of most common fluorescent dyes for biomolecules. Still, undoubtedly, the rejection issue adversely impacts the broader use of the contact geometry. Besides, the major remaining bottlenecks of both quantum dots and fluorescent dyes are their commonly met photo-instability, photobleaching and biological incompatibility, which have restricted their commercial biomedical applications.

Because they are free from such issues, non-bleaching and non-blinking lanthanide (Ln^{3+})-based upconversion nanoparticles (UCNPs), capable of converting near-infrared (NIR) photons into higher energy visible emission, are emerging as a new class for photoluminescence bioimaging probes [14–16]. Two key advantages for the synergy between UCNP and CMOS technology in fluorescence imaging are [17,18] (i) Silicon-based area CMOS detectors have lower quantum efficiency in the NIR range (less than 10%), compared with that in the visible range of upconversion luminescence (UCL) emission (above 50%), thus a positive factor for filter-free fluorescence imaging system; (ii) the long UCL lifetimes of UCNPs, from microseconds to even milliseconds, enable inexpensive time-gated detection schemes, capable of completely suppressing the excitation light or residual autofluorescence arising from the optical filters.

It is thus expected that combining superior UCNPs and CMOS properties may render biological analysis instruments low-cost, robust, compact and portable. In this paper, we present along this line a chip principle based on UCNPs, whose UCL lifetime can reach the millisecond range, but for which the excitation is at 975 nm, still well in the sensitivity window of silicon. Thanks to the long luminescence lifetimes, it is possible to expect a large part of the rejection ($>10^4$ to 10^6) by electronic means: Electronic shutters inside current fast-imaging CMOS sensor arrays can be active during the laser excitation and play the role of a very efficient rejection means. Such sensors typically target crash-tests for cars, with 50–100 μs exposure time as a lower limit and down to 200–250 μs frame time for 1000 pixel-area sub-images. We are not aware that such chips have yet been used for contact imaging, but since CMOS chips are commonly used in that contact format in niche technical applications (scintillators for X-ray imaging, notably dental imaging), we may reasonably assume that players in the micro-optoelectronics silicon industry shall as well produce fast chips compatible with contact imaging, the main issue being to contact the side pads more “horizontally”, and to adapt for instance a faceplate with the proper glue/resist combination.

So, as shown in Fig. 1(a), we can first hope that the electronic shutter rejection makes it possible to capture most of the upconverted photons emitted after a short excitation pulse, due to the long lifetime, without a *bona fide* spectral filter. Next, an optics-less contact version is straightforwardly deduced from this layout, as shown in Fig. 1(b) (compare to image 1(a) of Ref. [11] where a high-rejection filter is needed for standard fluorescence in the same compact lens-free biochip layout). It is well-known, however, that the usual multiphoton UCL efficiencies of Ln^{3+} -doped UCNPs are very low (typically $< 1\%$) and that the multicolor UCL emission, characterized by the electronic transitions of each Ln^{3+} ion (Er^{3+} , Tm^{3+} and Ho^{3+}) has a nonlinear response to excitation intensity (often power-law type). These characteristics normally result in a demand for high intensity. Fortunately, the high-intensity domain is not too

acute an issue because the excitation wavelength of 975 nm is among the best tolerated (minimal absorption) ones in biological media (cells and tissues). Nevertheless, it is always better to enhance the excitation intensity directly at or close to the useful surface where the useful signal is generated and to minimize said excitation intensity elsewhere on the path. To do this, a local-field enhancement provided by a resonant waveguide grating (RWG) structure was recently shown to achieve over 10^4 fold enhanced UCL emission from UCNPs [19,20]. A high degree of resonance on a waveguide at the chip surface can be obtained by a quite modest corrugation depth of the waveguide, a couple of 10's of nm, which makes the topology issue very secondary for most popular assays ("spots" of DNA biochips, or the various flavors of cell assays).

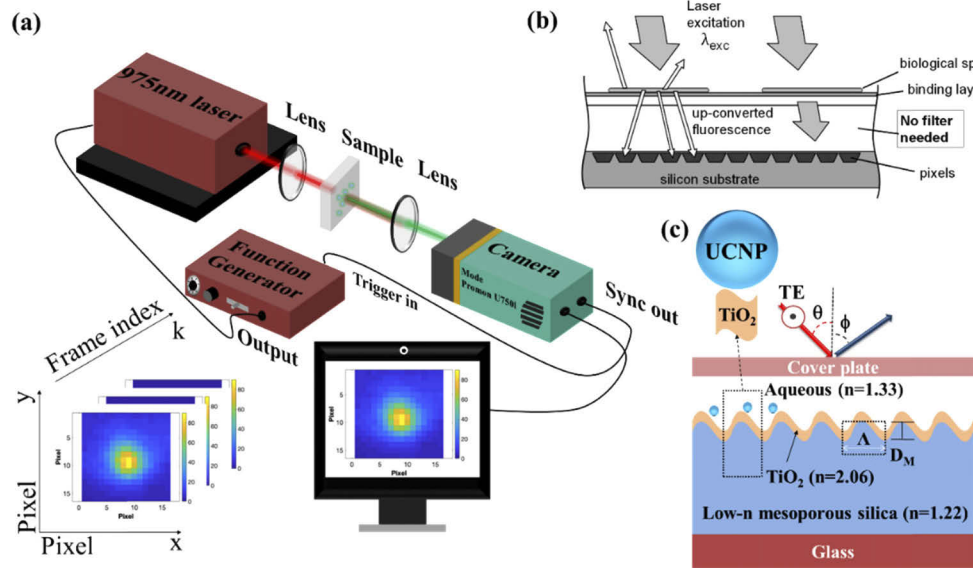


Fig. 1. Schematic of (a) the filter-free CMOS-based fluorescence imaging, (b) Lens-less compact scheme with contact geometry, compare with the filter-version of Ref. [11] for classical fluorescence; (c) the low-n RWG sample for enhancing UCL emission of UCNPs, reprinted with permission from Ref. [20].

Let us describe the main features of the setup of Fig. 1(a) that we shall use as a proof of principle of a contact-type, filter-free, lens-less chip geometry, as shown in Fig. 1(b). The CMOS chip-based fluorescence imaging was constructed based on a commercial high-speed camera (Promon U750, used with AOS imaging *studio v4* software). The excitation source for UCL measurement was a NIR fibered laser diode at 975 nm (common InGaAs-based model used to pump Erbium-doped fibers), which was synchronized with the detection window of the camera through a standard function generator (10 ns timing accuracy). The laser excitation time was set to $\tau_{pulse} = 50 \mu s$. The exposure (detection) time for a single detection window was set to $\tau_{det} = 100 \mu s$ for all measurement. Other details of the sequence will be given later in Section 5.

In another variant, in order to assess as much as possible the targeted lens-less chip geometry and the associated larger collection efficiency, we inserted directly a fiber optics plate (J3182-72, Hamamatsu) behind the sample. In the targeted lens-less geometry of Fig. 1(b), there would be, of course, a much larger collection $NA_{coll} \approx 1.0$, and a signal about 40 times larger than for $NA_{coll} \approx 0.15$, depending on the exact source emission diagram (e.g. Lambertian in a glass-type medium above the plate). However, with our setup and ordinary lenses, we lost a significant amount of upconverted photons. Only immersion microscope objectives would collect the full 1.0 aperture, to the expense of a reduced field. This alternative would have some heuristic interest,

but we believe that the simpler setup is a sufficient proof-of-principle, given the well-known properties of UCL emission in the targeted application (typically involving emission at transparent solid/aqueous medium interfaces).

To further enhance the UCL emission of UCNPs, as shown in Fig. 1(c), the best configuration is to use such a RWG for the 975 nm excitation wavelength around some prescribed angle of incidence, which matches the resonant angle of a guided-mode of the resonant grating. If the chip is excited in properly tuned optical conditions, the amount of transmitted (non-rejected) NIR light can become very small, assisting the aforementioned shutter rejection by the same token (and in addition to the differential sensor spectral sensitivity mentioned above). The main beam would be a reflected beam, while residual absorption in the waveguide would help “dumping” NIR photons and avert their undesirable scattering + detection on the image sensor.

In the following Section 2, we present the preparation process of UCNPs, including core, core-shell and core-shell-shell, which can be excited with a 975 nm laser source. In Section 3, we describe the principle in more detail and the extra uses that can be made of the various degrees of freedom. In Section 4, we discuss the photometric aspects and the kind of sensing performances that can be expected. In Section 5, we use the experiments in the far-field of Fig. 1(a) to assess the good rejection of the electronic shutter and other factors that are essential ingredients of the principle proposed in Fig. 1(b). We thus assess as much as possible the low limit of detection per pixel suggested by the system model, which turns out to be competitive with usual fluorophore down-conversion efficiencies. We conclude in the last section.

2. Materials and methods

2.1. Materials

Yttrium(III) chloride (YCl_3 , anhydrous powder, 99.99%), ytterbium(III) chloride (YbCl_3 , anhydrous powder, 99.9%), erbium(III) chloride (ErCl_3 , anhydrous powder, 99.9%), and ammonium fluoride (NH_4F , anhydrous 99.99%) were purchased from Sigma-Aldrich and stored in a dry box. Sodium hydroxide (pellets, 98%) was brought from Macron Fine Chemicals. Oleic acid (OA, technical grade, 90%) and 1-octadecene (ODE, technical grade, 90%) were purchased from Sigma-Aldrich.

2.2. Synthesis of outer shell (NaYF_4) solution

The outer shell precursor was initially prepared by mixing 1 mmol of YCl_3 , 6 mL of OA and 15 mL of ODE in a 100 mL round bottom flask. Under a nitrogen flow, the resulting mixture was then heated to 200°C to obtain a clear solution with a yellowish color. Next, the solution was placed under vacuum and heated to 110°C for 1 h to extract the unwanted impurities, then cooled down to room temperature. In the meantime, the fresh methanol solution was prepared by dissolving 0.1 g of NaOH and 0.148 g of NH_4F , followed by adding slowly into the reaction flask. Finally, the solution was heated at 110°C to extract methanol and then kept for the next stage.

2.3. Synthesis of middle shell ($\text{NaYF}_4:\text{Yb}$) solution

For the synthesis of the middle shell precursor solution, the procedure was the same as that for the outer shell except that YbCl_3 was used. Briefly, 6 mL of OA and 15 mL of ODE was mixed with 0.8 mmol of YCl_3 and 0.2 mmol of YbCl_3 in a 100 mL flask. Then, the mixture was heated to 200°C under a nitrogen flow with vigorous magnetic stirring. The clear solution was subsequently vacuum filtered and quickly heated to 110°C for 1 h. When the reaction solution is cooled down to room temperature, the methanol solution with 0.1 g of NaOH and 0.148 g NH_4F was added dropwise into the reaction flask. After removal of methanol by evaporation, the obtained solution was kept for further use.

2.4. Synthesis of core-shell-shell ($\text{NaYF}_4:\text{Yb,Er}@ \text{NaYF}_4:\text{Yb}@ \text{NaYF}_4$) UCNP

The $\text{NaYF}_4:\text{Yb,Er}$ core UCNP were initially synthesized as the protocol in our previous study [20]. Typically, 0.78 mmol of YCl_3 , 0.2 mmol of YbCl_3 , 0.02 mmol of ErCl_3 , 6 mL of oleic acid and 15 mL of ODE were mixed into a 100 mL flask, and heated to 200°C under a nitrogen atmosphere to obtain a transparent solution. Afterwards, the obtained solution was placed in a vacuum chamber and subsequently naturally cooled down to room temperature. Next, the methanol solution containing 0.1 g of NaOH and 0.148 g of NH_4F was added into the reaction. After removal of residual methanol, the reaction solution was heated to 300°C for 1 h and then cooled down to 280°C under a gentle flow of nitrogen gas. Subsequently, the solution of the middle shell precursor was added slowly at a speed of 0.05 mL/min, followed by adding the outer shell precursor in the same conditions. The mixture was allowed to react for another 15 min, and then rapidly cooled down to room temperature by blowing a stream of nitrogen at the outside of the reaction flask. Finally, the as-synthesized UCNP were collected by centrifugation at 6000 r.p.m for 10 min and washed with a mixture of cyclohexane/ethanol (1:1 v/v) at least two more times. After the last cycle, the as-obtained UCNP were redispersed in toluene for further experiments. For the synthesis of core-shell $\text{NaYF}_4:\text{Yb,Er}@ \text{NaYF}_4:\text{Yb}$ UCNP, the process was similar except the outer shell precursor (NaYF_4) was not used.

2.5. Characterization

The crystal structure of UCNP was determined with a Bruker APEX diffractometer ($\lambda = 1.5406 \text{ \AA}$). Morphology of nanoparticles was characterized with TEM (JEOL-JEM 2010). The optical measurements (UCL and lifetime spectra) were carried out using a home-built system, as described in Ref. [20].

2.6. Preparation of UCNP samples for fluorescence imaging

Typically, all as-synthesized UCNP samples (100 μL , 2 mmol/15 mL) were dropped onto glass substrates (2 cm \times 2 cm). Samples were then dried naturally at the room temperature.

3. Principle of excitation light rejection in the filter-free fluorescence imaging

3.1. Fluorescence from a square pulse

We first consider the setup of Fig. 1(a), without surface enhancement. The fluorescent species are UCNP (core, core-shell and core-shell-shell), with typical lifetimes τ_U in the range 100–2000 μs . The time-rejection issue is managed as follows. Consider an on/off square-shaped 975 nm NIR light pulse $I(t) = I_m \text{Rect}\left(\frac{t-t_0}{\tau_{\text{pulse}}}\right)$ centered at t_0 with a given peak intensity I_m and typically $\tau_{\text{pulse}} = 10 - 100 \mu\text{s}$. We assume that we have the response of UCNP as a collection of identical mono-exponential emitters with characteristic decay time τ_U . The physical UCL signal $I_U(t)$ at $t \geq t_0 + \frac{1}{2}\tau_{\text{pulse}}$ (after the pulse) can then be calculated according to a convolution:

$$\begin{aligned} I_U(t) &= \eta(I_m) \int_{-\infty}^t I(t') \exp\left(-\frac{t-t'}{\tau_U}\right) dt' \\ &= 2\eta(I_m) I_m \tau_U \exp\left(-\frac{t-t_0}{\tau_U}\right) \sinh\left(\frac{\tau_{\text{pulse}}}{2\tau_U}\right) \end{aligned} \quad (1)$$

with $\eta(I_m)$ being the adapted nonlinear upconversion efficiency (well defined for a constant-intensity pulse).

3.2. Window-detection of fluorescence imaging for a filter-free CMOS chip

The integrated UCL signal is integrated between two time bounds t_1 and t_2 . We write $t_1 = t_0 + \frac{1}{2}\tau_{\text{pulse}} + \tau_{\text{lag}}$, where τ_{lag} represents a lag-time after the end of the pulse at $t_0 + \frac{1}{2}\tau_{\text{pulse}}$, and

we write $t_2 = t_1 + \tau_{\text{exp}}$, where τ_{exp} is the exposure time, ideally defined by the electronic shutter. Both times t_1 and t_2 are *after* the end of the excitation pulse so that the integrated signal is given by:

$$F_U = \tau_U \tau_{\text{pulse}} \eta(I_m) I_m \sinhc\left(\frac{\tau_{\text{pulse}}}{2\tau_U}\right) \left[\exp\left(-\frac{t_1 - t_0}{\tau_U}\right) - \exp\left(-\frac{t_2 - t_0}{\tau_U}\right) \right] \quad (2)$$

with $\sinhc(x) = \sinh(x)/x$, the “sinc” function [$\text{sinc}(x) = \sin(x)/x$] but for the hyperbolic sine instead of normal sine. Compared to the maximum obtainable signal (all emitted photons) $F_{U\text{max}} = \tau_U \tau_{\text{pulse}} \eta(I_m) I_m$ (which is the convenient quantity to access to $\eta(I_m)$ in practice), we see that we obtain the fraction $F_U/F_{U\text{max}}$ defined by the last two factors. Defining $\alpha = \frac{\tau_{\text{pulse}}}{\tau_U}$, we note that $\sinhc\left(\frac{\alpha}{2}\right) \rightarrow 1$ when α vanishes. For instance, for the limit case $t_1 = t_0 + \frac{\tau_{\text{pulse}}}{2}$ ($\tau_{\text{lag}} = 0$) and $t_2 \rightarrow +\infty$, we obtain the fraction:

$$\frac{F_U}{F_{U\text{max}}} = \sinhc\left(\frac{\tau_{\text{pulse}}}{2\tau_U}\right) \exp\left(-\frac{\tau_{\text{pulse}}}{2\tau_U}\right) = \left(\frac{\tau_U}{\tau_{\text{pulse}}}\right) \left[1 - \exp\left(-\frac{\tau_{\text{pulse}}}{\tau_U}\right) \right] \quad (3)$$

whose *second-order* expansion in α is $1 - \frac{\alpha}{2} = 1 - \frac{\tau_{\text{pulse}}}{2\tau_U}$ (first-order is 1, the left-hand side expression with “sinhc” is indeed easier to grasp as none of its factors diverges): As can be intuited if the pulse is much shorter than the decay, about one half of the pulse width, $\frac{\tau_{\text{pulse}}}{2}$, becomes lost information if integration starts after the pulse, as if all the excitation energy had been deposited exactly at the pulse middle at t_0 and not distributed.

Thus, with a scheme featuring a 100 μs pulse width and a 1000 μs decay time, we shall still get 95% of available photons (and similarly for our 50 μs laser pulses and, say, a $\tau_U = 500$ μs decay time). Another case worth examination is $\alpha = 1$, thus $\tau_U = \tau_{\text{pulse}}$. Then we still get a fraction $1 - \frac{1}{e} = 0.63$ of the signal. To get only 25% of the signal (i.e. lose 75% due to the pulse duration), we have to assume $\tau_U \approx 0.57 \tau_{\text{pulse}}$, which is below 30 μs .

3.3. Lifetime retrieval feasibility

From the above analysis, we see that if we choose a shorter integration time, but perform several distinct integrations at well-chosen intervals $[t_1, t_2]$, we have several measurements for each pulse and we can *assess the lifetime of the measured species, in a large window* if signal-to-noise (SNR) is appropriately enhanced (on the one hand, measurements of weak signals are needed to assess the shorter decays, cf. Equation (3), on the other hand, longer decay times for a given excited population means a lower photon flux).

3.4. Enhanced rejection with lagged detection

We also see from the general formula Eq. (2) for detection after the pulse that we have some margin to delay the shutter exposure by the lag time τ_{lag} , say by 10's of μs . This delay may be favorable to rejection, as trapped photocharges from the intense excitation pulse may survive in the sensor during a very short shutter time and induce spurious signal. Some extra delay helps recombining or de-trapping these charges. Such an advantage can be favorably traded-off with a 2-10% decay of the useful signal. We will give experimental data on the impact of this lagged detection.

4. Photometric aspects

4.1. Photometric aspects of the setup

Let us give more photometry-related features for the setup, Fig. 1(a): A convex 35 mm doublet lens was used to focus the laser output onto a $\sim 20 \mu\text{m}$ diameter spot in order to increase excitation light local intensity for generating stronger UCL emission from UCNPs. The emitted UCL signal was then collected by another lens (50 mm focal length, 25 mm diameter, thus numerical

collection aperture $NA_{\max} \approx 0.25$) and delivered to the image sensor of the camera through its standard objective set at infinity, and whose 15.5 mm outer pupil (f-number 1.4) restricts the beam and defines the actual collection efficiency at the sample as $NA_{\text{coll}} \approx 0.15$. The camera was connected to a computer using the USB 3.0 port for imaging acquisition and hardware installation. The camera + software enables frame rates up to 6000 frames per second (fps) at the 16×16 pixel frame and still 4000 fps for 32×32 pixel frames. All data were analyzed by an *ad hoc* program written in Matlab, which readily allows the signal analysis of captured images. We use the software camera counts, associated to an 8-bit digitization scheme.

4.2. Photometric aspects of the lens-free + RWG detector

Very-high rejection and high sensitivities would be needed if operation at moderate power is desired, say less than 20 mW incident power in the near-infrared. To alleviate this, we can recourse to guided mode resonance (GMR) enhancement of RWG structure. It was demonstrated that the UCL intensity of Tm^{3+} -doped UCNP has strongly enhanced signal by utilizing RWG structures, higher than 10^4 -fold those in PMMA matrix [19] or aqueous solution [20]. This demonstration involved Q factors that are only in the range 400-1000, thanks to the UCL response being highly nonlinear ($Q=10^4$ would have been needed for linear response). Also, the coupling was not yet perfect (the optimal coupling depends notably on the losses), as the residual transmission at the peak was generally above 60%.

We further deal here with two points that are of importance for the actual signal: the photon paths from assay to sample, and the range of signal that has to be reached to operate on ordinary room-temperature CMOS sensors, assuming state-of-the-art noise figures for the photodiodes.

We have treated mathematically the assay above as a “black box” with excitation as input and fluorescence as output. One should keep in mind that extraction efficiencies are a very important factor in actual efficiencies. Here, the main point is to channel the F_U photons of Eq. (2) to the sensor.

We write the number N of UCL photo-electrons per pulse and per pixel as the following product: $[\text{Excitation power density}] \times [\text{Absorption cross section per UCL}] \times [\text{UCL concentration}] \times [\text{Pixel Area}] \times [\text{Excitation efficiency in RWG}] \times [\text{Extraction efficiency on the bottom side}] \times [\text{Collection efficiency in } NA=1] \times [\text{Detector sensitivity}]$.

The last three factors of this expression are assumed to reach 0.2 in total. We consider a pixel area, say $10 \times 10 \mu\text{m}$, and assume a coupled power of 10 mW along an elongated broad line of $10 \mu\text{m}$ width in the RWG (assuming for instance a residual transmission of 40% and 10% reflection, this means a 50% excitation efficiency in RWG, the fifth factor of the formula, and fits the 20 mW excitation power suggested above, the important data is the coupled power). For optimal use, the absorption should be 100% over the typical light path of $\ell = Q \times \text{wavelength}$ ($Q \sim 1000$) in the RWG's guide, so say $\ell = 400 \mu\text{m}$ and thus 2.5% absorption of guided beam within $10 \mu\text{m}$. This deposits 250 μW per pixel, which become with 0.4% UCL efficiency 1 μW of blue-green light. This gives 2.5×10^{12} photons/s hence about 1.25×10^9 photons in 500 μs (typical detection time and fluorescence time as well). There are thus, with the three last factors taken as 0.2, $N = 2.5 \times 10^8$ photo-electrons per pulse, which is still 5×10^3 over a reasonable typical room-temperature noise floor of 5×10^4 electrons. So the detection limit would be as low as 10^{-3} of the concentration $C_{400\mu\text{m}}$ that causes an absorption length of NPs of $400 \mu\text{m}$ for a guided mode.

Theoretically, the absorption cross-section of Yb^{3+} ion is about $1.15 \times 10^{-20} \text{ cm}^2$ at 980 nm [21]. A unit cell of the β -phase NaYF_4 -based UCNP has lattice parameters: $a = 0.591 \text{ nm}$, $c = 0.353 \text{ nm}$, as reported in Ref. [22]. Therefore, if we model a CSS UCNP as a regular hexagonal prism shaped single crystal having the above average lattice parameters and the following size: base edge length $a_{\text{UCNP}} = 50 \text{ nm}$ and height $h_{\text{UCNP}} = 25 \text{ nm}$ (see Section 5 below), it contains 1.317×10^6 unit cells. It is also well-known that a unit cell of NaLnF_4 contains two Ln^{3+} ions (including: 78% of Y, 20% of Yb, 2% of Er), which dictates as much as 5.27×10^5 Yb ions per

UCNP particle, and a naive 980 nm cross section of $\sigma_{UCNP} \approx 6.06 \times 10^{-15} \text{ cm}^2$. To go further, we need a guided mode data, say a typical vertical squared-field profile of effective height $h_{wg} \approx 300 \text{ nm}$ in typical RWG waveguides. A layer of 25 nm thickness ($=h_{UCNP}$) with 1 particle every $a_{pix} = 10 \mu\text{m}$ (pixel size), overlapping a guided mode with vertical confinement factor $\Gamma \sim h_{UCNP} / h_{wg}$ of about 0.08, is a heuristic limit case. The guided beam effective cross section above the pixel being $a_{pix}h_{wg} \approx 3 \times 10^{-8} \text{ cm}^2$, the single particle attenuates the beam by a factor $\sigma_{UCNP} / (a_{pix}h_{wg}) = 2 \times 10^{-7}$. To reach the above mentioned criterion of $10^{-3} \times 2.5\% = 2.5 \times 10^{-5}$ attenuation, it is thus sufficient to have 125 UCNP's per pixel. We thus claim, given the margin that can still be improved, that the detection limit of this room-temperature scheme is rather in the 10-100 UCNP's per pixel, which compares well with standard fluorescence labels. Coarsely speaking, the RWG geometry and the high Q can compensate for the lower efficiency of UCNP's.

For CSS UCNP's experiments below, we drop-casted 100 μL of CSS solution dispersed into toluene (77 mg/mL) onto the glass substrate ($2 \text{ cm} \times 2 \text{ cm}$). As reported in Ref. [22], the UCNP's with a size of 100 nm have a molecular weight of 10^3 MDa , corresponding to $1.66 \times 10^{-12} \text{ mg/particle}$. This resulted in an average concentration of $1.16 \times 10^{10} \text{ particles/mm}^2$. Other kinds of UCNP's (core and core-shell) were prepared with the same molar concentration of CSS UCNP's, which have the same particle density. The spot size of the focused 975 nm laser excitation beam is $20 \mu\text{m}$, leading to look at around 4.6×10^6 UCNP's in one spot, equivalent to 1.4×10^6 per pixel. However the last factors are lower than the "ideal" value 0.2 by 1-2 orders of magnitude at least (among other things there are no RWG), so a limit of detection is rather expected around 10^4 UCNP's per pixel in our case. We defer the detailed optical figure of merit and precise noise-floor estimates to further work and will only discuss below the broad agreement with the above estimates.

5. Results and discussion

5.1. Characterization of UCNP's

The basic structural (TEM, XRD) characterization results of the three kinds of UCNP's are shown in Figs. 2(a)–2(b) and their upconversion fluorescence spectra in Fig. 2(c). We also investigated the decays of UCL emission at the dominant green emission ($^4\text{S}_{3/2} \rightarrow ^4\text{I}_{15/2}$ transition) see Fig. 2(d). The measured UCL lifetime, τ_m , is determined by the rate at which the ions leave their excited state, which can be written as a combination of the radiative transition rate ($1/\tau_R$) and non-radiative relaxation rate (W_{NR}), according to the following equation:

$$\frac{1}{\tau_m} = \frac{1}{\tau_R} + W_{NR} \quad (4)$$

Figure 2(d) clearly displays that the UCL lifetime was effectively extended from 258 μs (core) to 686 μs (core-shell), resulting from the prolongation of the diffusive energy migration of Yb^{3+} ion [23]. With the further addition of the inactive shell, an even longer green emission lifetime, 979 μs for CSS UCNP's, was observed under 976 nm excitation. In fact, the growth of an inert shell possessing similar material with interior core does not result in the significant change in local crystal field surrounding the dopants, so the radiative rate ($1/\tau_R$) is the same for both CS and CSS UCNP samples. As a result, the longer lifetime at each UCL emission peak observed in the CSS-structured UCNP's indicates the lower non-radiative relaxation rate [23–26], which agrees with the result shown in Fig. 2(d). These long luminescence lifetime, highly efficient UCNP's are ideal to serve as photoluminescence probes for ultra-compact filter-free bio-assays.

5.2. Detector rejection vs. lag time

As a proof-of-concept, a proposed home-build imaging system based on CMOS-chip high-speed camera can be used to assess both UCL emission and lifetime modes of UCNP's, as introduced

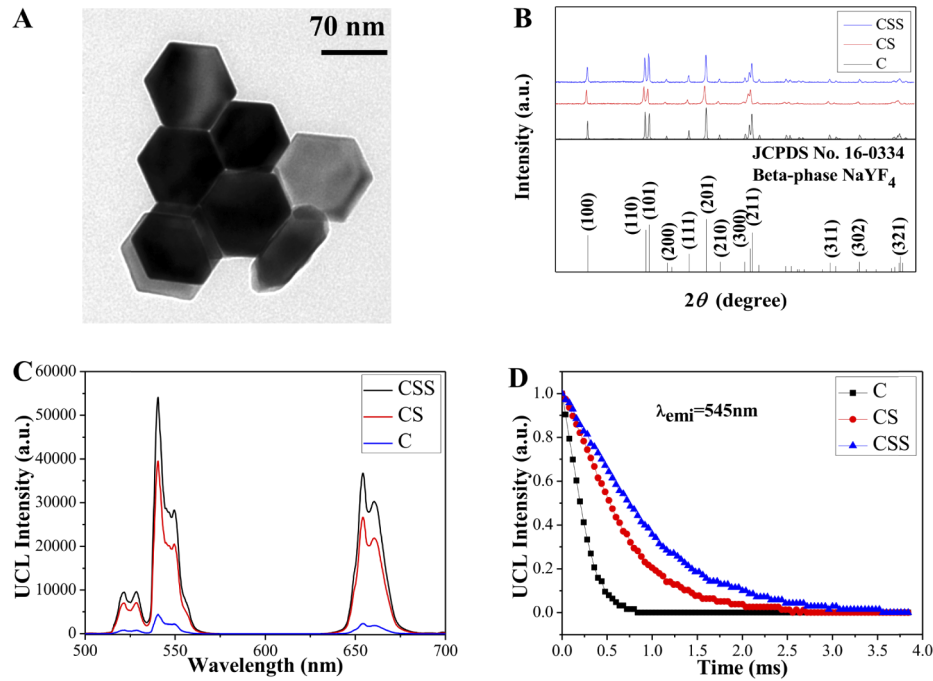


Fig. 2. Characterization of UCNPs. (A) TEM image of $\text{NaYF}_4:\text{Yb}^{3+},\text{Er}^{3+}@\text{NaYF}_4:\text{Yb}^{3+}@\text{NaYF}_4$ CSS UCNPs. (B) XRD pattern of C, CS, CSS samples and standard beta-phase NaYF_4 data (JCPDS file no. 16-0334). (C) UCL emission spectra in the wavelength range of 500-700 nm of the as-synthesized samples (C, CS, CSS) under 976 nm excitation. (D) Lifetime measurement of the UCL emission at 545 nm obtained from C, CS, CSS samples.

in Fig. 1(a). Figure 3(a) illustrates the timing diagram for the operation of filter-free CMOS chip-based fluorescence imaging. A NIR fibered laser diode with a wavelength of 975 nm was used as an excitation source, which can be modulated at the desired frequency with negligible transients. Here we typically operate with frame time of $\tau_{\text{frame}} = 200 \mu\text{s}$, thus at 5000 fps: the high-speed camera allows this rate for a small but arbitrary-located 16×16 pixel frame with $\tau_{\text{exp}} = 100 \mu\text{s}$ exposure. The control signal for the excitation light is synchronized with the detection window gate in the image sensor. We essentially want to adjust the lag time τ_{lag} and detection (electronic shutter open) duration τ_{exp} as indicated in Fig. 3(a). A negative τ_{lag} corresponds to the laser being still on during the exposure interval. We take several images after each pulse to evaluate both intensity and decay of UCL emission. Technically, we use the sync signal of the camera to trigger through the function generator the next pulse with a long delay which is a large multiple of the frame time plus a shift of a fraction of the period. For simplicity, we focus on this sole fractional shift that we call τ_{lag} . All in all, in this measurement, the 975 nm laser source eventually delivers an average power of 0.12 mW with a 50 μs pulse width at a repetition rate of only 50 Hz, providing a time interval between the subsequent pulses of 20 ms with $N_{\text{post}} = 100$ post-pulse frames after each pulse.

On the physics side, the background signals on a glass substrate were first recorded at the same camera conditions later used for the measurement of UCL emission, with the laser being either off (dark noise signal) or on (excitation background signal, without UCNP), to find the optimal conditions for image acquisition and assess the degree of non-ideal camera shuttering. Note that the signal was collected and directed to the image sensor in the camera by a lens at an off-axis

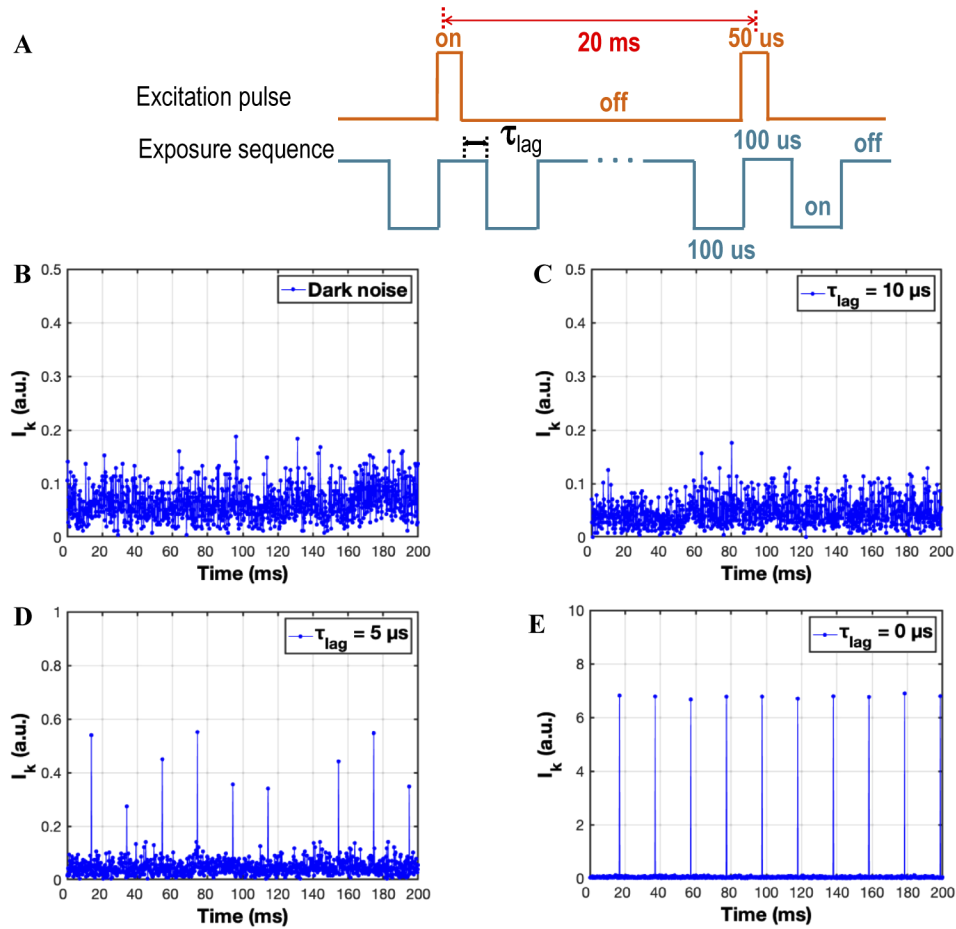


Fig. 3. Impact of excitation light at short lags for a glass substrate (no UCNP) due to the non-ideal shuttering: (a) Timing diagram for the operation of filter-free CMOS chip-based fluorescence imaging. The average pixel intensity histogram of the detected signal curve plotted over recorded time, obtained from (b) dark noise, laser excitation "noise" at the different τ_{lag} : (c) 10 μs , (d) 5 μs , (e) 0 μs .

angle relative to the laser direction to reduce excitation light delivered to the camera (On-axis measurements are addressed below in Section 5.5). An average pixel intensity for each of the frames, hereafter referred to as $I_{x,y,k}$, was determined by averaging all x - y addresses of pixels in the image sequence, according to the equation:

$$I_k = \frac{1}{N_{pixel}} \sum_{x=1}^{16} \sum_{y=1}^{16} S(x, y, k) \quad (5)$$

where x, y are pixel coordinates, k is the frame index, $N_{pixel} = 256 = 16^2$ and $S(x, y, k)$ represents the pixel signal. Figures 3(b)–3(e) show the average pixel intensities for all captured frames and plot it over time, allowing the evaluation of dark and excitation noises. It clearly evidences that the excitation light signal captured at $\tau_{lag} = 10 \mu s$ (Fig. 3(c)) remains on the order of the dark noise on the image sensor (see Fig. 3(b)). As τ_{lag} was decreased, the scattered light from the excitation pulse is seen at all the corresponding frames, $k = k_0 + mN_{post}$ ($m = 0$ to 10 here, $k_0 < N_{post}$ is an experimental offset), giving rise to an increase of light captured in a single exposure detection window. This signal is about 10 times the dark noise at $\tau_{lag} = 5 \mu s$ (with large fluctuations) and becomes ~ 140 times the dark noise at $\tau_{lag} = 0 \mu s$, now in a very reproducible fashion. It is likely that trapped photoelectrons generated in the camera chip during the laser pulse are de-trapped within a time scale of $1 \mu s$ or less so that after $10 \mu s$, no signal can be detected (a multi-exponential signal is likely for such trapping, but its analysis goes beyond the scope of this paper, and is probably very much camera-specific, in spite of the numerous common features of CMOS technologies in different foundries). Therefore, a choice such as $\tau_{lag} = 10 \mu s$ ensures that the excitation pulse can be totally rejected in this off-axis configuration (we will provide a corresponding statement for the on-axis case below), hence a promising first step for the filter-free CMOS chip-based imaging. This value was thus chosen for the next step for recording the UCL signal of UCNPs.

5.3. Upconversion filter-free measurements

As a short-pulsed NIR excitation source irradiates a specimen which carries upconversion nanoprobes, the subsequent emission light of high-energy photons in the visible region will be generated, which have a long exponential decay on the order of milliseconds. For the fluorescence imaging acquisition using traditional photoluminescence probes, i.e., organic dyes or quantum dot, with rapid exponential decay, typical nanosecond to several tens of nanoseconds, the excitation light must be filtered out by a high-rejection optical filter to ensure only the desired fluorescence light is collected on the image sensor or detector. In this study, the background signal associated with the NIR excitation beam was effectively eliminated by the proper selection of detection time window of the high-speed camera. Taking the advantages of the long luminescence rise and decay times associated with UCNPs, the capture of UCL signal was performed after the excitation pulse. This electronic shuttering allows the high rejection of the excitation light and negligibly penalizes the high collection efficiency of UCL emission light time-wise, as was discussed in the mathematical model (Sections 3.2–3.3).

The timing principle of UCL measurements based on the filter-free fluorescence imaging is outlined in Fig. 4(a). According to the aforementioned calibration of the background noise, the capture conditions, such as the laser pulse-width of $50 \mu s$, the exposure sequence of $100 \mu s$ and the delay (τ_{lag}) of $10 \mu s$ were chosen as the guideline for the measurement of UCL emission signal. By counting all pixel intensity values within every captured window of a 10 pulse sequence of 200 ms (1000 frames), a luminescence decay curve can be deduced. Here we average on the $N_{frame} = 10$ frames that have the same n -th post-pulse position in the sequence, i.e.

$k = k_0 + mN_{post} + n$, which is associated with the decay “instant” $\tau = n\tau_{frame} = n \times 200 \mu\text{s}$:

$$I_\tau = \frac{1}{N_{frame}} \frac{1}{N_{pixel}} \sum_{m=1}^{N_{frame}} \sum_{x=1}^{16} \sum_{y=1}^{16} S(x, y, k_0 + mN_{post} + n) \quad (6)$$

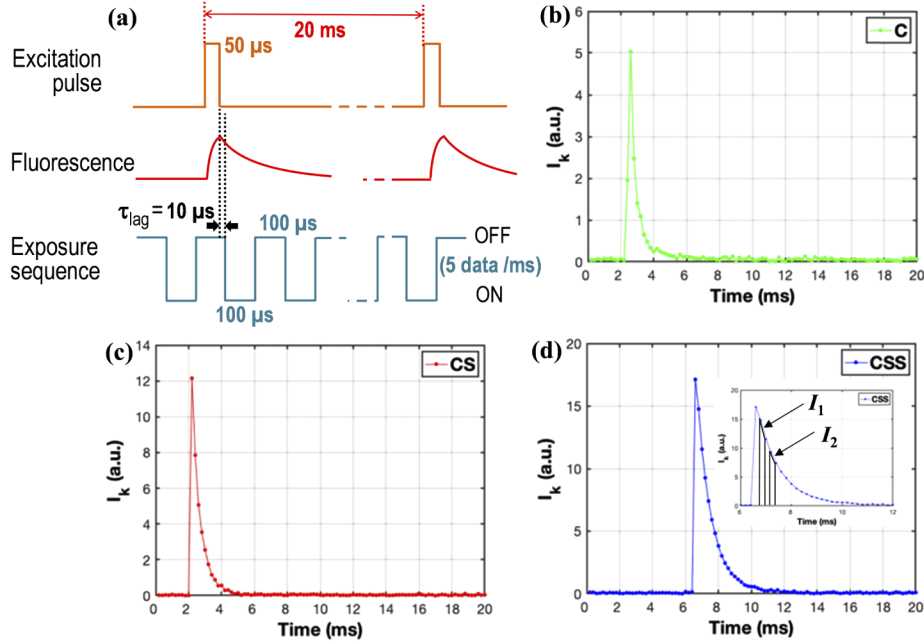


Fig. 4. (A) Timing diagram for the operation of filter-free CMOS chip-based fluorescence imaging. The average intensity histogram of the detected signal curve plotted over recorded time, obtained from (B) core, (C) core-shell, (D) core-shell-shell UCNPs at $\tau_{lag} = 10 \mu\text{s}$.

Figures 4(b)–4(d) reveal the intensity and decay of the UCL emission obtained from the upconversion samples (C, CS and CSS). By comparing the peak values for each sample, it confirms that the UCL intensity of CSS UCNPs is the strongest among these samples (17 vs. 12 for CS and 5 for C), the same trend as the UCL spectra displayed in Fig. 2(c). The time-integrated values $\int I_\tau d\tau$, akin to the number of emitted photons, display an even stronger trend (85 for CSS vs. 36 for CS vs. 12 for C). Furthermore, given the high SNR ratio, the UCL lifetime can be calculated here from the ratio of the luminescence intensities within two adjacent count windows N_1, N_2 as shown in the inset of Fig. 4(d), as expressed in the following equation:

$$\tau = \frac{\Delta T}{\ln(I_1/I_2)} \quad (7)$$

where ΔT represents the time interval between two time gates with equal width, I_1 and I_2 are the integrated luminescence intensity within the corresponding time gates, respectively. Analysis of these decay curves yielded lifetime estimations of 875, 534 and 350 μs for the core, core-shell, core-shell-shell structured UCNPs, respectively, which are close to the measured lifetimes displayed in Fig. 2(d). These results prove the feasibility to obtain direct UCL imaging without the need for an optical filter, providing a powerful tool for high-throughput imaging with the high rejection ratio of background. A contact imaging device would have exactly the same timing behavior, only the photometric issues would be different (and more favorable to

emission collection). We note that the large margin vs. noise observed here are compatible with the various estimates made in Section 4, and thus make it more plausible that an attainable detection limit of the lens-free contact scheme is indeed in the 10-100 UCNPs per pixel range.

5.4. Cross-check of infrared rejection

To confirm the high amount of UCL signal captured in our design and technique (excitation attenuation, negligible noise and low-cost), and in particular the very limited impact of the lag time on this amount, we devised a way to collect the highest possible UCL emission intensity from UCNPs in this generic scheme, which is expected for $\tau_{lag} = 0 \mu s$. To this end, we recorded the signal within two photometric configurations, with and without using a standard excitation filter (KG5, cutting the NIR), since the situation with filter is insensitive to excitation at any time in the sequence. Figure 5(a) shows the luminescence decay curve obtained from CSS UCNPs in the filter-free photometric at $\tau_{lag} = 0 \mu s$, where the falling edge of the excitation pulse coincides with the start of the exposure window. Compared with the result obtained at $\tau_{lag} = 10 \mu s$ (Fig. 4(d)), the signal intensity of the former is much higher than that of the latter, indicating that a high amount of pumping light had illuminated the image sensor and created photo-carriers that were able to show up as a signal in the detection window.

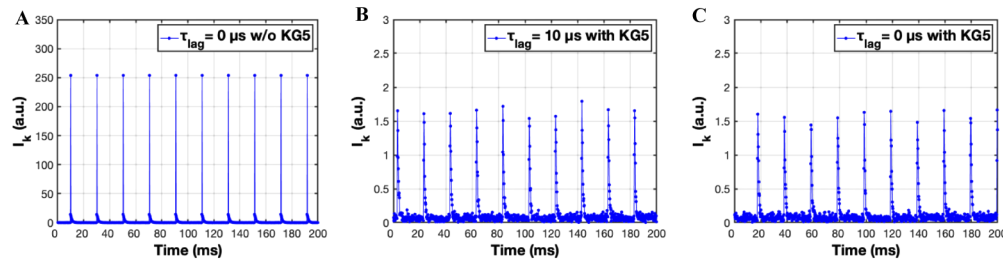


Fig. 5. The average intensity histogram of the detected signal curve plotted over recorded time, obtained from CSS UCNPs at (a) $\tau_{lag} = 0 \mu s$ w/o KG5, (b) $\tau_{lag} = 10 \mu s$ with KG5, (c) $\tau_{lag} = 10 \mu s$ with KG5.

To determine how the UCL signal is affected by the addition of the $10 \mu s$ lag time, we compare UCL imaging for both lag times with the KG5 filter inserted, getting rid of any NIR light. As shown in Figs. 5(b) and 5(c), the light intensity captured for both cases is entirely similar, both being much weaker compared with that obtained without the KG5 filter and $\tau_{lag} = 0 \mu s$. The filter has a certain effect to attenuate the spectrum in the region of UCL emission. The similar amount of signal at $\tau_{lag} = 10 \mu s$ implies that the UCL emission light is significantly captured with negligible loss. Besides confirming the theory for simple exponential decay that predicts a $< 2\%$ impact, an extra factor favourable for the unchanged signal could be the long rise time of UCNPs luminescence [27], that facilitates its centering in the exposure window. Its modelling is a refinement that would, however, introduce complexities that we do not need for our central claims.

5.5. On-axis geometry

Next, we study the fluorescence imaging of UCL by the camera at an on-axis angle of incidence. We do this study in the absence of a RWG or any «light» rejection filter such as a simple Bragg mirror. A good RWG or a few-layers Bragg mirror could reduce the NIR transmission by a factor of 10. So our study is clearly a *worst case*: almost all NIR photons of the laser reach the sensor given the various apertures involved. The 975 nm diode laser is pulsed at a repetition rate of 83.3 Hz with an average power of 110 μW and a pulse duration of 50 μs (peak power is thus 26.4 mW). The high-speed camera is now set to acquire images at a frame rate of 250 fps

(thus $N_{post} = 3$) with the detection time window of 100 μs . This choice allowed to treat more signal-containing frames than the previous $N_{post} = 100$ choice. The delay time is set to ensure the same $\tau_{lag} = 10 \mu\text{s}$ as in the previous experiments under the off-axis geometry. Figures 6(a) and 6(b) display the intensity traces from glass substrate and CSS UCNPs, respectively. The signal is about 10 times larger in the latter case. So, there are now photocarriers generated by the laser and seen later in spite of the 10 μs lag (the laser is completely off after at most a fraction of μs , being regulated by a current source with sufficient bandwidth and undergoing a large transient). To evaluate a precise SNR ratio in this situation, we must subtract the laser signal from the total signal. The important quantities are thus the standard deviation of each signal. As can be seen in the histograms of 200 peaks of Figs. 6(c) and 6(d) that relate to the glass substrate and CSS case respectively, both signals have a similar standard deviation: it is characterized by a FWHM width $\Delta S_{FWHM} = 0.20$ in both cases. This is likely to be a readout noise, as it is only 2–4 times larger than the dark noise seen in the above section. In our conditions, the inhomogeneity of the image may play a role in the exact value of such quantities and may result in such modest discrepancies. The important point is the equal value of both width and the sufficient plausibility of a Gaussian distribution. It means that the standard deviation and FWHM width of the difference signal that represents the upconversion luminescence ($S_{UCL} = S_{CSS} - S_{glass}$) are only multiplied by $\sqrt{2}$. The FWHM width thus reaches 0.28 and the standard deviation 0.12 ($\approx 0.28/2\sqrt{2\ln 2}$). Hence the UCL signal to standard deviation (“noise”) ratio is $\sim 15/0.12$ and exceeds 100 in this experiment, where a large part of the unwanted excitation signal turns out to be deterministic.

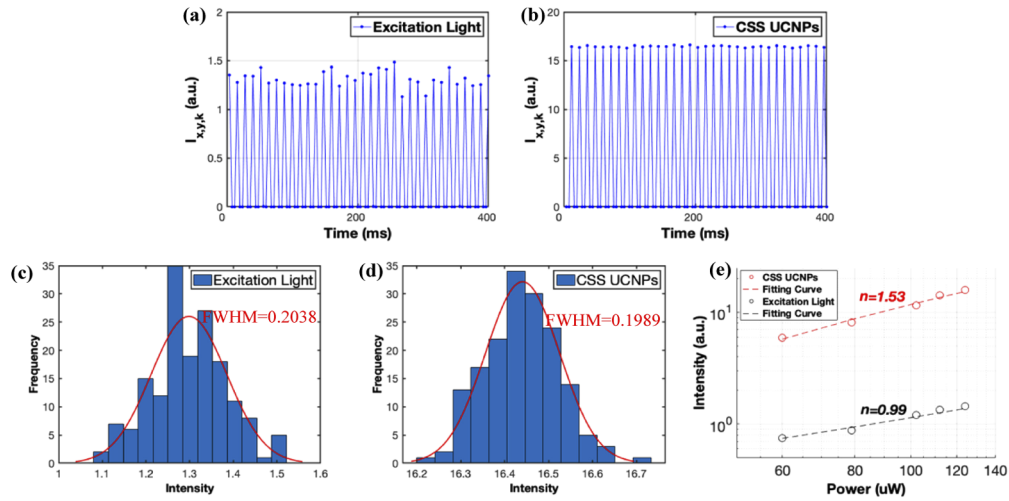


Fig. 6. On-axis geometry : The average image intensity records (150 fps, 83.3 Hz laser), obtained from (a) glass sample (only excitation light), (b) CSS UCNPs. Intensity histograms for the signals from (c) excitation light and (d) CSS UCNPs, showing identical fitted Gaussian width of 0.20. (e) Log-log plot of signal dependence on incident power (we use the average power as measured, the peak power is stronger by a factor 400 for these 50 μs pulses every 20 ms). The nonlinearity of UCNP signal (obtained by subtraction) with fitted exponent $n=1.53$ is clear, while it is near unity for excitation light.

To cross-check the origin of the UCL emission, it is appropriate to verify the non-linear property of UCL emission. We thus studied the excitation intensity dependence of the UCL emission intensity of the UCNPs sample by repeating the experiment for five different excitation powers (P_{exc}) in the range of 60–130 μW . The UCL emission intensity emitted from UCNPs was again inferred by subtracting the laser background (as in Fig. 6(a)) from the detected signal (as

in Fig. 6(b)), $S_{UCL}(P_{exc}) = S_{CSS}(P_{exc}) - S_{glass}(P_{exc})$. Figure 6(e) displays the log-log plot of the inferred signal intensities $S_{UCL}(P_{exc})$ and $S_{glass}(P_{exc})$ versus the excitation P_{exc} . It is observed that $S_{UCL}(P_{exc})$ is proportional to the n th power of the excitation power, where the fitted exponent n is 1.5 for the UCL emission from CSS UCNP associated with a theoretical two-photon process of the transitions of erbium ions. For comparison, $S_{glass}(P_{exc})$ shows the fitted exponent n of 0.99, with the various noise sources plausibly accounting for the minute difference to unity.

We thus observe that the technique is robust to the situation of the chip geometry. Even a head-on laser beam with typically 40 mW can be accommodated with a background that does not harm the dynamical range appreciably, and with also a still very modest and entirely tractable contribution to the standard deviation. Let us again insist that this is a worst-case: In the targeted geometry of a chip, the increased collection efficiency of UCL with an aperture of 1.0 (faceplate aperture) compared to 0.15 here should bring a 30 to 40-fold improvement, while an optimized GMR mode of the RWG would reduce the NIR excitation beam by a factor of 10. With this factor of 300 margin, and with the increased signal excitation enhancement of 10^4 due to the RWG grating field concentration, we have a factor over 2×10^6 at hand, ideally. We can thus hope that a single pixel (or pixel group) can detect 10 NPs instead of an estimated $\sim 3 \times 10^4$ in our test experiments (inferred from the fact that we currently have 5×10^6 UCNP in the imaged spot and a UCL to noise ratio over 100, however, we did not undertake concentration-dependent experiments that are more delicate to perform). This broadly agrees with the lines of theoretical calculation as presented in Section 4.2. We believe that on this basis, our technique will find applications in small, robust and low-cost fluorescence-based devices.

5.6. Prospective imaging performance of the face optic plate

Our technique has shown the high excitation light rejection characteristics in the filter-free, lens-less CMOS-based fluorescence imaging, however, there is still room for further improving the performance of this microscopy platform. To evaluate the feasibility of using this fluorescence imaging technique for contact imaging and RWG detector, we performed the measurement with slight modifications. One emerging possibility toward lens-free contact imaging is the use of an additional planar optical component, i.e. a fiber optic faceplate (FOP) inserted directly after the sample substrate as illustrated in Fig. 7(a). In this modified configuration, the rapid divergence (free space propagation modes) of UCL emission from specimen is converted into the guided modes of a 2D array of fiber-optic bundles without spatial spreading, thanks to the high numerical aperture (up to 1.0) [6,7,28,29]. Because such chips have not yet been prepared for contact imaging, we performed a simple test to estimate the spot width captured by the camera. The imaging system is kept the same as in Fig. 1(a), except insertion of the FOP between the sample and the sensor. In addition, to excite UCL emission generated from UCNP, the 975 nm laser beam coupled to this setup has an off-angle (θ) with respect to the surface normal direction. This configuration is a simulation for the resonant excitation condition of RWG structure, i.e. the incident angle and wavelength of the excitation light simultaneously matching with the resonant angle and wavelength of a guided-mode of the RWG. Note that the image size was kept at 32×32 frame, whereas the other experimental conditions for the camera and laser pulse were similar to the study in Section 5.5.

In order to evaluate the imaging performance of our lens-free on-chip technique, the signals from excitation light and CSS UCNP were captured and analyzed at different lag times. Figure 7(b) displays the particular images of the measured spots obtained from the CSS UCNP sample at the different indicated lag times. Each image averaged on 168 frames was analyzed by an *ad hoc* program written in Matlab. It clearly shows that the detected spot is larger and brighter as τ_{lag} decreases to negative values, as a consequence of trapping of the laser excitation signal in the exposure window. At the positive value $\tau_{lag} = 5.87 \mu s$, it exhibits a bright spot corresponding to the UCL signal, and a relatively weak background laser noise. Conversely, the UCL signal is

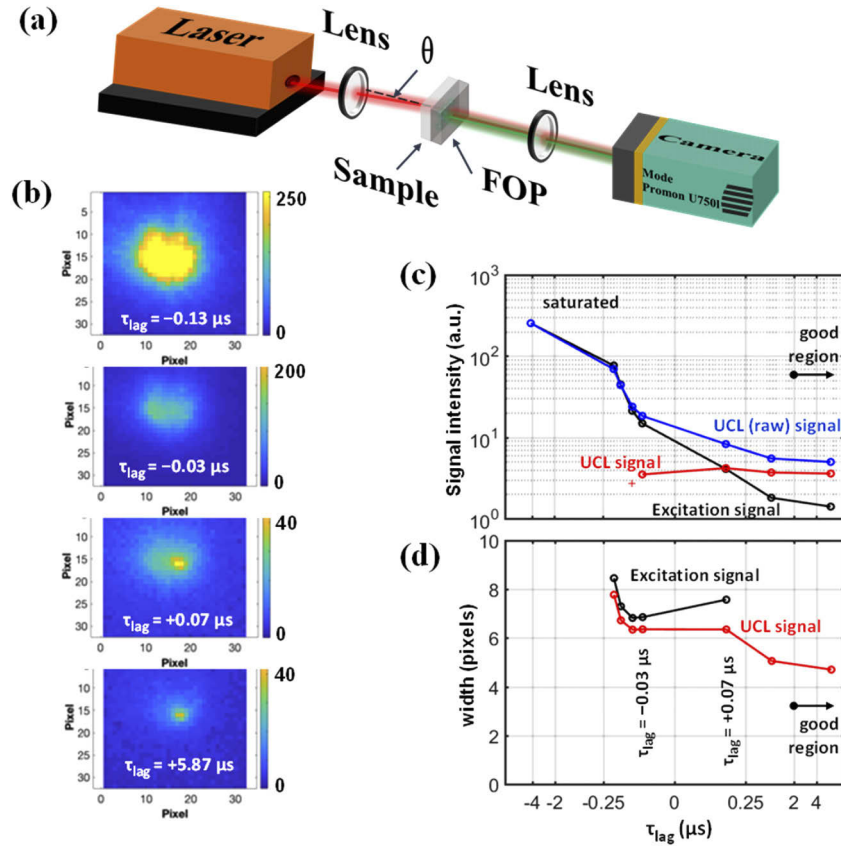


Fig. 7. Experiments with a Fiber-Optics-Plate added (a) Schematic of the filter-less CMOS-based fluorescence imaging with the FOP. θ is the excitation beam incident angle relative to the FOP + sample surface normal direction. (b) Images of the signal obtained from the CSS samples, averaged on 168 frames, at indicated lag times. (c, d) Laser-only and CSS UCNP data vs. lag time τ_{lag} . The lag time τ_{lag} is purposely indicated on a very nonlinear horizontal scale [$X \propto \tau_{lag}^{1/4} \times \text{sign}(\tau_{lag})$]: (c) The average intensities for the signals from CSS UCNP sample (blue curve) and excitation light (black curve), and the difference (red curve). (d) The peak typical width for excitation light (black curve) and for CSS UCNP sample (red curve).

indistinguishable from the laser noise at negative τ_{lag} . It implies that by selecting the proper τ_{lag} , we can filter out excitation light efficiently.

Hereafter, we use an adapted abscissa $X = \tau_{lag}^{1/4} \times \text{sign}(\tau_{lag})$ with exponent $1/4$ arbitrarily chosen to give a gently stretched rendering of the transition for the exposure window starting either before ($\tau_{lag} < 0$, $X < 0$) or after ($\tau_{lag} > 0$, $X > 0$) the end of the laser pulse. Figure 7(c) makes use of this abscissa to depict a quantitative comparison of the average pixel intensities for the excitation-only signal (black curve) and raw UCL emission (blue curve) signals. The red difference curve shows the signal that comes from the sole UCL and is constant to better than 5% in the two rightmost data points here. It suggests that beyond a positive τ_{lag} as small as 1 μs , there is an insignificant change in the captured intensity of the raw UCL emission signal.

The widths of the signal spots of the aforementioned samples were also analyzed by a numerical method using Matlab. The intensity distribution in each imaging spot displayed in Fig. 7(b) was fitted to a Gaussian lineshape model to extract a proper account of spot width. Figure 7(d) shows the width of the signal spot of the excitation light (black curve) and CSS UCNP sample (red curve) as a function of the same stretched abscissa X as above. We analyzed the measured signals before they were saturated at $\tau_{lag} = -4.13 \mu\text{s}$. According to the numerical analysis of the laser and UCL emission signals at the negative τ_{lag} , both yield similar widths as the laser signal dominates. Width variations are observed from CSS UCNP sample between different τ_{lag} , which are attributed to variations in the number of UCL photons captured in the exposure window. As the UCL signal dominates, the spot width is smaller than that of the laser spot and closer to the system resolution (about 100 μm). The results suggest that the optimal region of the lag time for capturing the UCL emission signal should start after about 4 μs to ensure the characteristics of high-efficient UCL detection and high excitation light rejection. The evolution of the recorded signal clearly displays the advantages of our technique especially in terms of excitation light rejection.

Besides, the imaging spot of the UCL signal still remains relatively small without a noticeable penalty in the degradation of UCL intensity with the use of the FOP, which is a good starting point for our further study of the filter-free optics-less system. Therefore, contact imaging using dense FOP to collect and deliver UCL emission from sample to image sensor without the use of any lenses is the next approach to achieve high throughput and small spatial resolution. Another advantage of tuning the incident angle is to eliminate the appearance of shadow of the microbiological specimen on the image sensor, thus improving the sensitivity of image in the bright field (non-fluorescent imaging) [28].

Such novel imaging architecture combining the long UCL lifetime of UCNP and the high-speed imaging capabilities of the camera could be especially valuable for high-throughput imaging, compactness, and low-cost systems expanding fluorescence-based analysis.

6. Conclusion

Herein, we present the new concept of synergy between UCNP and fast (1–100 μs) CMOS imaging technology for achieving filter-free, lens-less fluorescence imaging at a modest cost. By taking the key characteristics and advantages of long UCL emission and high-speed imaging capabilities, we demonstrate the feasibility for fluorescence detection with both off- and on-axis excitation geometries. In our fluorescent imaging technique, the samples of interest are pumped through the 975 nm excitation source, whose excitation pulse is synchronized with, and prior to, the detection window of the camera. By choosing the proper lag time between the laser pulse and the detection window, a high-rejection of the excitation light can be achieved while UCL collection remains excellent. Another benefit of using UCNP as fluorescence nanoprobe is the long decay time (possibly assisted by a non-negligible rise time), which results in an efficient collection of UCL signal into the exposure window of the camera. Furthermore, multiple images in the sequence are useful: By the analysis of the luminescence intensities of Ln^{3+} -doped UCNP

at our available rates, the UCL lifetime can be assessed, showing very good agreement with the otherwise measured UCL lifetime, a neat way to control signals. Further investigation of coupling a FOP or fiber-optic-plate into the fluorescence system was also performed, revealing the high potential for the next step in contact imaging and combination with RWG detector. Such a compact fluorescent imaging platform is expected to enable the ubiquitous, inexpensive and high-performance imaging systems, which can open a new avenue of fluorescence imaging assays.

Funding

Agence Nationale de la Recherche (ANR-17-CE09-0047); Ministry of Science and Technology, Taiwan (107-2923-M-194-001-MY3, MOST-107-2923-M-194-001-MY3).

Disclosures

All other authors declare that they have no competing interests.

References

1. X. Zhang, A. Fales, and T. V. Dinh, "Time-resolved synchronous fluorescence for biomedical diagnosis," *Sensors* **15**(9), 21746–21759 (2015).
2. Y. Fan, S. Wang, and F. Zhang, "Optical multiplexed bioassays improve biomedical diagnostics," *Angew. Chem. Int. Ed.* **58**(38), 13208–13219 (2019).
3. F. Wang, S. Wen, H. He, B. Wang, Z. Zhou, O. Shimoni, and D. Jin, "Microscopic inspection and tracking of single upconversion nanoparticles in living cells," *Light: Sci. Appl.* **7**(4), 18007 (2018).
4. T. Lagache, A. Grassart, S. Dallongeville, O. Faklaire, N. Sauvonnet, A. Dufour, L. Danglot, and J. C. O. Marin, "Mapping molecular assemblies with fluorescence microscopy and object-based spatial statistics," *Nat. Commun.* **9**(1), 698 (2018).
5. L. Wei, W. Yan, and D. Ho, "Recent Advances in fluorescence lifetime analytical microsystems: contact optics and CMOS time-resolved electronics," *Sensors* **17**(12), 2800 (2017).
6. A. F. Coskun, I. Sencan, T. W. Su, and A. Ozcan, "Lensless wide-field fluorescent imaging on a chip using compressive decoding of sparse objects," *Opt. Express* **18**(10), 10510 (2010).
7. K. Sasagawa, A. Kimura, M. Haruta, T. Noda, T. Tokuda, and J. Ohta, "Highly sensitive lens-free fluorescence imaging device enabled by a complementary combination of interference and absorption filters," *Biomed. Opt. Express* **9**(9), 4329 (2018).
8. B. R. Rae, K. R. Muir, Z. Gong, J. Mckendry, J. M. Girkin, E. Gu, D. Renshaw, M. D. Dawson, and R. K. Henderson, "A CMOS time-resolved fluorescence lifetime analysis micro-system," *Sensors* **9**(11), 9255–9274 (2009).
9. E. Petryayeva and W. R. Algar, "Toward point-of-care diagnostics with consumer electronic devices: the expanding role of nanoparticles," *RSC Adv.* **5**(28), 22256–22282 (2015).
10. S. Nayak, N. R. Blumenfeld, T. Laksanasopin, and S. K. Sia, "Point-of-care diagnostics: recent developments in a connected age," *Anal. Chem.* **89**(1), 102–123 (2017).
11. L. Martinelli, H. Choumane, K. N. Ha, G. Sagarzazu, T. Gacoin, C. Goutel, C. Weisbuch, and H. Benisty, "Sensor-integrated fluorescent microarray for ultrahigh sensitivity direct-imaging bioassays: Role of a high rejection of excitation light," *Appl. Phys. Lett.* **91**(8), 083901 (2007).
12. A. Pandya, I. Schelkanova, and A. Douplik, "Spatio-angular filter (SAF) imaging device for deep interrogation of scattering media," *Biomed. Opt. Express* **10**(9), 4656 (2019).
13. C. Richard, A. Renaudin, V. Aimez, and P. G. Charette, "An integrated hybrid interference and absorption filter for fluorescence detection in lab-on-a-chip devices," *Lab Chip* **9**(10), 1371 (2009).
14. C. Chen, C. Li, and Z. Shi, "Current advances in lanthanide-doped upconversion nanostructures for detection and bioapplication," *Adv. Sci.* **3**(10), 1600029 (2016).
15. M. Lin, Y. Zhao, S. Q. Wang, M. Liu, Z. F. Duan, Y. M. Chen, F. Li, F. Xu, and T. Lu, "Recent advances in synthesis and surface modification of lanthanide-doped upconversion nanoparticles for biomedical applications," *Biotechnol. Adv.* **30**(6), 1551–1561 (2012).
16. W. Zheng, P. Huang, D. Tu, E. Ma, H. Zhu, and X. Chen, "Lanthanide-doped upconversion nano-bioprobes: electronic structures, optical properties, and biodetection," *Chem. Soc. Rev.* **44**(6), 1379–1415 (2015).
17. L. Wei, S. Doughan, Y. Han, M. V. DaCosta, U. J. Krull, and D. Ho, "The intersection of CMOS microsystems and upconversion nanoparticles for luminescence bioimaging and bioassays," *Sensors* **14**(9), 16829–16855 (2014).
18. A. Nadort, V. K. A. Sreenivasan, Z. Song, E. A. Grebenik, A. V. Nechaev, V. A. Semchishen, V. Y. Panchenko, and A. V. Zvyagin, "Quantitative imaging of single upconversion nanoparticles in biological tissue," *PLoS One* **8**(5), e63292 (2013).

19. J. H. Lin, H. Y. Liou, C. D. Wang, C. Y. Tseng, C. T. Lee, C. C. Ting, H. C. Kan, and C. C. Hsu, "Giant enhancement of upconversion fluorescence of $\text{NaYF}_4\text{:Yb}^{3+}, \text{Tm}^{3+}$ nanocrystals with resonant waveguide grating substrate," *ACS Photonics* **2**(4), 530–536 (2015).
20. D. T. Vu, H. W. Chiu, R. Nababan, Q. M. Le, S. W. Kuo, L. K. Chau, C. C. Ting, H. C. Kan, and C. C. Hsu, "Enhancing upconversion luminescence emission of rare earth nanophosphors in aqueous solution with thousands fold enhancement factor by low refractive index resonant waveguide grating," *ACS Photonics* **5**(8), 3263–3271 (2018).
21. Y. F. Wang, G. Y. Liu, L. D. Sun, J. W. Xiao, J. C. Zhou, and C. H. Yan, " Nd^{3+} -sensitized upconversion nanophosphors: Efficient *in vivo* bioimaging probes with minimized heating effect," *ACS Nano* **7**(8), 7200–7206 (2013).
22. L. E. Mackenzie, J. A. Goode, A. Vakurov, P. P. Nampi, S. Saha, G. Jose, and P. A. Milner, "The theoretical molecular weight of $\text{NaYF}_4\text{:RE}$ upconversion nanoparticles," *Sci. Rep.* **8**(1), 1106 (2018).
23. J. Zuo, D. Sun, L. Tu, Y. Wu, Y. Cao, B. Xue, Y. Zhang, Y. Chang, X. Liu, X. Kong, W. J. Buma, E. J. Meijer, and H. Zhang, "Precisely tailoring upconversion dynamics via energy migration in core-shell nanostructures," *Angew. Chem. Int. Ed.* **57**(12), 3054–3058 (2018).
24. F. Zhang, R. Che, X. Li, C. Yao, J. Yang, D. Shen, P. Hu, W. Li, and D. Zhao, "Direct imaging the upconversion nanocrystal core/shell structure at the subnanometer level: Shell thickness dependence in upconverting optical properties," *Nano Lett.* **12**(6), 2852–2858 (2012).
25. Y. Wang, L. Tu, J. Zhao, Y. Sun, X. Kong, and H. Zhang, "Upconversion luminescence of $\beta\text{-NaYF}_4\text{:Yb}^{3+}, \text{Er}^{3+}$ @ $\beta\text{-NaYF}_4$ core/shell nanoparticles: Excitation power density and surface dependence," *J. Phys. Chem. C* **113**(17), 7164–7169 (2009).
26. S. Fischer, N. D. Bronstein, J. K. Swabeck, E. M. Chan, and A. P. Alivisatos, "Precise tuning of surface quenching for luminescence enhancement in core-shell lanthanide-doped nanocrystals," *Nano Lett.* **16**(11), 7241–7247 (2016).
27. K. Green, K. Huang, H. Pan, G. Han, and S. F. Lim, "Optical temperature sensing with infrared excited upconversion nanoparticles," *Front. Chem.* **6**, 416 (2018).
28. K. Sasagawa, S. H. Kim, K. Miyazawa, H. Takehara, T. Noda, T. Tokuda, R. Iino, H. Noji, and J. Ohta, "Dual-mode lensless imaging device for digital enzyme linked immunosorbent assay," *Proc. SPIE* **8933**, 89330N (2014).
29. A. F. Coskun, I. Sencan, T. W. Su, and A. Ozcan, "Wide-field lensless fluorescent microscopy using a tapered fiber-optic faceplate on a chip," *Analyst* **136**(17), 3512 (2011).